References and Notes

1. M. Prather *et al.*, in *Climate Change 1994*, J. T. Houghton *et al.*, Eds. (Cambridge Univ. Press, New York, 1995), pp. 73–126.
2. This data is from the National Oceanic and Atmospheric Administration/Climate Monitoring and Diagnostics Laboratory air sampling network (available at www.cmdl.noaa.gov/ftpdata.html).
3. D. M. Etheridge, G. I. Pearman, F. de Silva, *Ann. Glaciol.* **10**, 28 (1988).
4. M. A. K. Khalil and R. A. Rasmussen, *ibid.*, p. 73.
5. D. Zardini *et al.*, *J. Atmos. Chem.* **8**, 189 (1989).
6. M. Leuenberger and U. Siegenthaler, *Nature* **360**, 449 (1992).
7. T. Machida *et al.*, *Geophys. Res. Lett.* **22**, 2921 (1995).
8. J. Chappellaz *et al.*, *Nature* **366**, 443 (1993).
9. T. Blunier *et al.*, *ibid.* **374**, 46 (1995).
10. J. Chappellaz *et al.*, *J. Geophys. Res.* **102**, 15987 (1997).
11. For the N_2O measurements the refreezing temperature was held at −25°C.
12. The extraction causes a loss of $(2.32 \pm 0.47) \times 10^{-8}$ ml of N_2O (at standard temperature and pressure), corresponding to a concentration correction of about 6 ppbv with a typical sample size of 40 g of ice.
13. The enrichment due to gravitational fractionation is 1.5 ppbv for the GRIP samples from the past millennium and 1.7 to 2.3 ppbv for the other GRIP samples. The Byrd samples have to be corrected by 1.0 to 1.1 ppbv. The results presented here have not been corrected.
14. R. G. Prinn *et al.*, in *Trends '93: A Compendium of Data on Global Change*, T. A. Boden, D. P. Kaiser, R. J. Sepanski, F. W. Stoss, Eds. (ORNL/CDIAC-65) (Carbon Dioxide Information Analysis Center, Oak Ridge National Laboratory, Oak Ridge, TN, 1994), pp. 396–420.
15. M. Battle *et al.*, *Nature* **383**, 231 (1996).
16. W. Dansgaard *et al.*, *ibid.* **364**, 218 (1993).
17. T. Blunier *et al.*, *ibid.* **394**, 739 (1998).
18. A surplus of N_2O could be caused by a chemical reaction in the ice, as in the case of CO_2 [M. Anklin, J.-M. Barnola, J. Schwander, B. Stauffer, D. Raynaud, *Tellus* **47 B**, 461 (1995); H. J. Smith, M. Wahlen, D. Mastroianni, K. Taylor, P. Mayewski, *J. Geophys. Res.* **102**, 26577 (1997)] and CO [D. Haan and D. Raynaud, *ibid.* **50B**, 253 (1998)]; a postcoring effect (for example, because of the infiltration of bore hole liquid into micro cracks); or an analytical artefact. We remeasured a sample from the same depth range, 0.07 m deeper in the core than that with the highest N_2O concentration, and again obtained about the same value (410 and 397 ppbv, respectively). This test rules out an accidental error or contamination during extraction and analysis, but it does not rule out the possibility that N_2O could be produced during the extraction in the melt water because of chemical impurities or a postcoring effect. We observed that the artefacts are very local in the ice core; a third measurement 0.51 m deeper in the core than the highest result showed a value of 283 ppbv. The same effect was observed in four other cases. At present, we cannot identify any reactions that would produce N_2O in the meltwater or in the ice.
19. K. Fuhrer *et al.*, *Atmos. Environ.* **27A**, 1873 (1993).
20. J. Schwander *et al.*, *J. Geophys. Res.* **102**, 19483 (1997).
21. C. Kroeze, A. Moiser, L. Bouwman, *Global Biogeochem. Cycles* **13**, 1 (1999).
22. The calculations were made with a one-box atmospheric model [M. A. K. Khalil and R. A. Rasmussen, *Ann. Glaciol.* **10**, 73 (1988)].
23. A. F. Bouwman *et al.*, *Global Biogeochem. Cycles* **7**, 557 (1993).
24. J. E. Dore *et al.*, *Nature* **396**, 63 (1998).
25. For the Monte Carlo simulation, 1000 runs were simulated. Each run takes into account the fact that the deviations from the mean values show a Gaussian distribution and calculates a smoothed spline with a cutoff period of 300 years [I. G. Enting, *J. Geophys. Res.* **92**, 10977 (1987)]. The 1σ band is given by the mean and the standard deviation of all splines.
26. S. J. Johnsen *et al.*, *Nature* **359**, 311 (1992).

27. This work, as part of GRIP, was supported by the University of Bern, the Swiss National Science Foundation, the European Community program "Environment and Climate 1994–1998," the Fondation de France, and the Programme National d'Étude de la Dynamique de Climat. Special thanks to J. Schwander, F. Joos, and R. Knutti for fruitful conversations and to E. Wolff and two anonymous reviewers for constructive comments.

5 February 1999; accepted 4 June 1999

Optical Vortices Crystals: Spontaneous Generation in Nonlinear Semiconductor Microcavities

J. Scheuer and M. Orenstein

Broad-area, vertical-cavity surface-emitting lasers were shown to switch their emission mode from the regular single or multilobed light fields to exhibit complex arrays of "dark beams." Examination of these dark spot arrays revealed that they consist of multiple, closely packed optical vortices: optical fields that have phase singularities and show increased complexity as the injection current level is raised. Contrary to their complex appearance, most of these light distributions are not the result of a multimode (multiple-frequency) operation but exhibit single-frequency characteristics. The dark beam patterns can be described as emanating from a spontaneous process of transverse mode locking of nearly degenerate modes, assisted by the laser nonlinearity. Surprisingly, these patterns show high resemblance to patterns generated in other nonlinear scenarios that are completely different both in scale and in mechanism.

The formation and propagation of complex, transverse, spatiotemporal field patterns (dynamically evolving optical field patterns, manifested as a complex structure of high- and low-intensity areas across the optical beam) in nonlinear optical devices is both of a fundamental interest and could have applications in a variety of areas such as optical data storage, distribution and processing [exploiting the robustness of a vortex field (*1*)], and laser cooling [optical trapping of particles in the featured intensity distribution (*2*)]. The generation of global field patterns was explored recently in optical cavities incorporating a nonlinear medium (*3–6*). These studies focused mainly on externally driven cavities and exhibited the formation of ordered patterns of bright or dark spots with hexagonal symmetry. Other patterns, such as rolls (repeated elongated field distributions), had been observed as well (*3*). The experimental observation of these phenomena is intricate because of the requirement for high values of both the Fresnel number and the nonlinearity. As a result, "optical crystals" were observed mainly in hybrid electro-optical systems [systems that mimic a performance of an optical structure by replacing some of its more difficult-to-achieve intrinsic mechanisms (such as nonlinearity and feedback) with an electronic realization] and also in a nonlinear macrocavity containing sodium vapor (*7*).

Semiconductor microcavities under lasing condition are potentially the best microlaboratories for producing and using complex optical fields because of the reasons detailed here. These devices combine a very high-quality optical cavity and a nonlinear medium. The semiconductor laser nonlinearity is of a saturation type and is unique in having an appreciable contribution from both the real and imaginary nonlinear index of refraction. The intrinsic gain of the laser assists in overcoming the losses that are a dominant factor in the deterioration of the nonlinear propagation. The vertical cavity configuration plays a major role in the pattern formation discussed

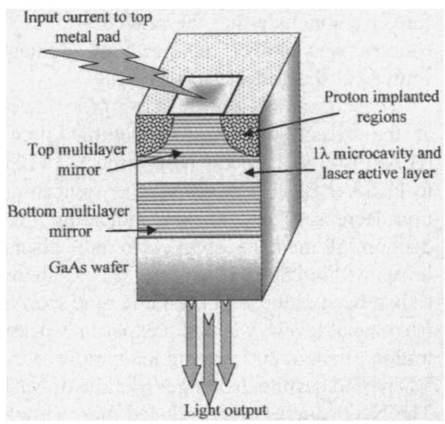

Fig. 1. Schematics of the nonlinear microcavity cross section.

Department of Electrical Engineering, Technion, Haifa 32000, Israel.

here. First, it has a very large Fresnel number: The cavity mirror separation is only a single wavelength but the lateral dimensions are many wavelengths. The second factor is its two-dimensionality, as compared to the one-dimensionality of regular semiconductor lasers (the latter emit from their edge and by construction—one of their lateral dimensions is tightly bounded by an epitaxially grown waveguide). The two-dimensionality is a critical constituent in the generation of the vortex arrays discussed below, because vortices cannot be formed in one-dimensional systems. Finally, the nonlinear microcavity is a miniature, easily fabricated, and easily controlled (by injection current) device. We show that the microcavity of a vertical-cavity semiconductor laser, which is usually used as a conventional-mode (Gaussian-like bright beam) light source, can also serve as a micrononlinear source of stable complex transverse patterns.

The vortex arrays were studied in broad-area, vertical-cavity surface-emitting lasers (VCSELs) (cylinders with a diameter $D = 20$ μm and box cavities with areas of 20 μm by 20 μm, both with a mirror spacing of one wavelength). These emitters were grown by molecular beam epitaxy to form microcavity lasers with three 8-nm $In_{0.2}Ga_{0.8}As$ quantum wells as the active layer and an emission wavelength of ~985 nm. Although the effective lateral cross section was a circle or a square, the actual lateral structure was mechanically unbounded, and the lateral extent was limited only by protons implanted into the semiconductor structure to define the current path (*8*) (Fig. 1). The lasers were examined under continuous wave (CW) conditions at injection currents from 7 to 43 mA. The near-field intensity pattern was imaged through the thinned laser wafer both directly on a charge-coupled device (CCD) and through a spectrometer to obtain the spectrally resolved near-field intensity patterns.

As the injection current was increased over 15 mA, the near-field lasing pattern switched from narrow, bright light filaments (Fig. 2) to complex patterns characterized by arrays of "dark" peaks rather than the grid of "bright" peaks of a conventional mode. These dark peaks were shown to be optical vortices of absolute charge 1. We denote an optical field distribution as a dark beam when there is an intensity notch characterized by a definite cross section (a beam) embedded in a higher intensity background. An optical vortex is a specific case of a dark beam (*4, 9*) for which the phase of the electrical field experiences a singularity at the center of the beam. For a physically realizable field, its absolute amplitude must vanish at this point. The order of the singularity, denoted also as the charge of the vortex, is calculated as the circulation of the phase gradient about the singularity $\oint \nabla\Phi \cdot dl = 2\pi m$ (the residue theorem). The integer m is the topological charge of the vortex.

The first complex pattern to emerge (16 mA) (Fig. 3) was a figure eight–like pattern consisting of two equal charge vortices followed by a four-vortex array (17.2 mA) and a radial symmetric pattern (20 mA). Increasing the current further (above 25 mA) caused patterns of a higher complexity to evolve, as depicted in Fig. 4, consisting of arrays of three, five, and seven vortices. Imaging of these patterns through a spectrometer to get the spectrally resolved near-field distribution indicated that each of these patterns was a single-mode emission rather than a combination of lasing modes, as might have been expected from these large-area emitters. The theoretically predicted results are also shown in Figs. 3 and 4 and are in good agreement with the experimental observations.

Changing the pumping parameter of the microcavity laser to even higher current levels (above 30 mA) resulted in increased complexity (some field distributions are shown in Fig. 5), including single-frequency patterns with a large number of vortices (up to 19) as well as multiwavelength patterns. The latter incoherent patterns preserved the highly regular crystallike near-field distribution (*10*). Optical systems have not previously generated such a large number of vortices, and they were generated here within a very small cross section—20 μm in diameter. The beam width of each vortex was less than 1 μm.

In order to verify the nature of the dark beams, an interference experiment was conducted. A portion of the VCSEL emission was spatially filtered to generate a plane

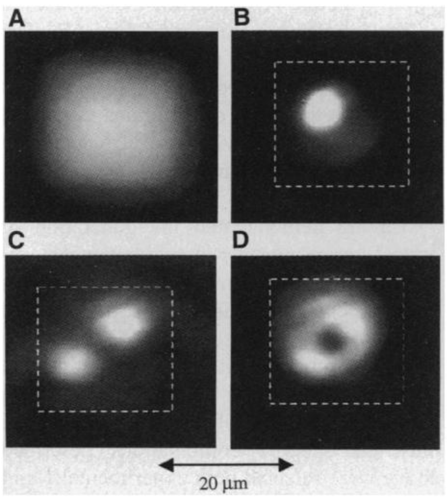

Fig. 2. Light filaments (bright beams) at low injection currents. (**A**) Spontaneous emission, (**B**) a single filament, (**C**) two coupled filaments, (**D**) doughnut mode.

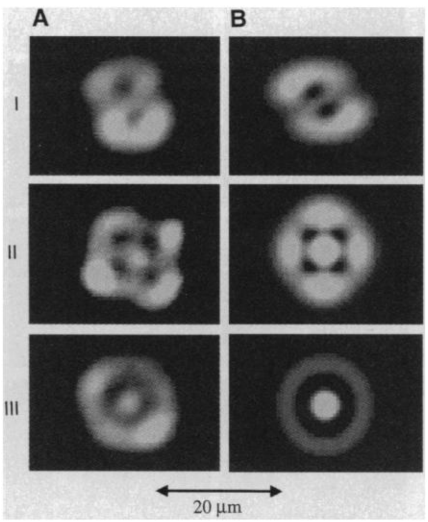

Fig. 3. Transverse pattern for the second ($2p + l = 2$) pattern band: experimental (**A**) (I, 16 mA; II, 17.2 mA) and theoretical (**B**) [I, $\sigma \sim 1.5, J_o \sim 1 \times 10^{-17}$; II, $\sigma < 0.7, J_o \sim 3 \times 10^{-17}$; III, $\sigma > 3, J_o > 4 \times 10^{-17}$ (J_o units, A/μm^2)].

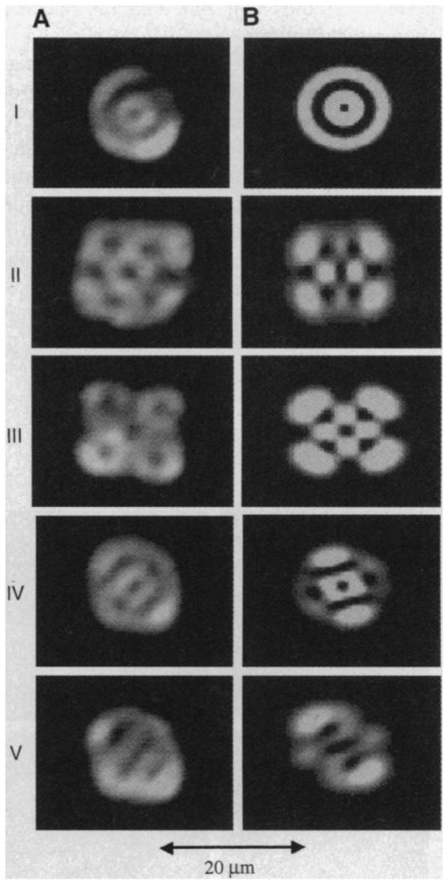

Fig. 4. Transverse pattern for the third ($2p + l = 3$) pattern band: experimental (**A**) (I, 25 mA; II, 26.3 mA; III, 27.8 mA; IV, 28.2 mA; V, 28.6 mA) and theoretical (**B**) [I, $\sigma \sim 3, J_o \sim 1.5 \times 10^{-17}$; II, $1.3 < \sigma < 1.4$, $2 \times 10^{-17} < J_o < 2.5 \times 10^{-17}$; III, $1 < \sigma < 1.5$, $2.5 \times 10^{-17} < J_o < 2.8 \times 10^{-17}$; IV, $\sigma \sim 1, J_o \sim 2.5 \times 10^{-17}$; V, $\sigma \sim 1.1, J_o \sim 3 \times 10^{-17}$ (J_o units A/μm^2)].

wave reference beam. The VCSEL near-field pattern and the reference beam were interfered on a CCD imager plane. As mentioned above, an optical vortex stems from a helical phase distribution with a phase jump of $2\pi m$ (*9*). Thus, the interference pattern of a vortex and a plane wave exhibited the appearance or disappearance of m fringes at the vicinity of the vortex singularity. Figure 6A depicts the experimentally measured interference patterns of some of the vortex arrays emitted by the VCSEL (I, "doughnut" mode; II, figure eight pattern; III, four-vortex array; and IV, seven-vortex array). The structure of the interference patterns reaffirmed that the dark beams were field singularities with an absolute charge of 1. Further confirmation was obtained by comparing the experimental interference to the synthetic interference of the calculated emitted fields (Fig. 6B).

By measuring the far-field distribution, we observed that the complex patterns preserved the lateral functional structure in the far field as well. Thus, not only the total singularity charge was preserved in free space propagation [which is expected from previous studies (*1*)] but also the specific charge distributions.

The theoretical study of the pattern formation was performed by exploring the microcavity laser rate equations (*11*), coupled to the nonlinear Maxwell's wave equation describing the transverse fields. Reducing these equations using paraxial field propagation and a steady-state assumption resulted in a complex Ginzburg Landau (CGL)–like equation with a saturation type nonlinearity

$$\frac{\partial \varepsilon}{\partial t} = i \cdot \frac{c^2}{2 \cdot \omega_0 \cdot n^2} \cdot \nabla^2 \varepsilon - \frac{c}{n} \cdot \alpha_{tot} \cdot \varepsilon + \frac{c}{n} \cdot \Gamma \cdot (1 - i \cdot R) \cdot \frac{g_0}{1 + |\varepsilon|^2 / E_{sat}^2} \cdot \varepsilon$$

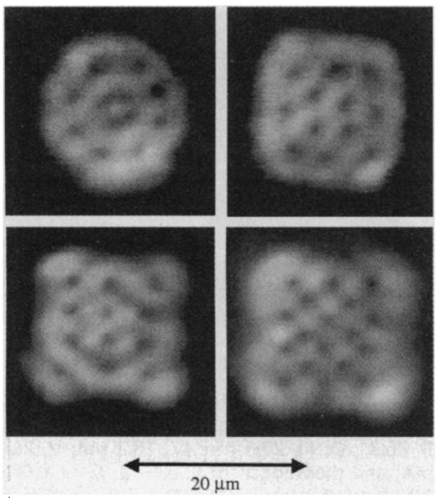

Fig. 5. Experimental near-field lasing patterns of higher families and incoherent patterns. I > 30 mA.

where ε is the electrical field, g_0 is the small signal gain, c is the speed of light, n is the refractive index, Γ is the confinement factor, R is the antiguiding factor, and E_{sat}^2 is the gain saturation intensity. The CGL equations with cubic and quintic nonlinearity were shown previously to exhibit vortex solution (*9*). Furthermore, we showed in closed form (*12*) that the semiconductor microcavity system under lasing conditions, satisfying the above CGL equation, could spontaneously yield both bright and dark soliton solutions. These observations were the cornerstone of our ability to demonstrate both bright filaments (bright solitons) and vortex arrays (dark soliton combinations) from the same device by tuning the control parameter.

In order to explore the specific mechanism of the onset of the complex dark beam arrays, we examined the family of cold cavity modes contributing eventually to the nonlinear formation of the pattern. Our structure consisted of a short but wide cavity that was weakly laterally confined by the current aperture (no mechanical boundaries). The modes of the linear cylindrical cavity are similar to the hybrid modes obtained for cylindrical waveguides (*13*). This set consists of bands of closely spaced modes (~0.01 nm of intraband separation for the guiding parameters of our structure) with interband wavelength spacing of ~0.1 nm as was actually measured in our experiments. We expect that the role of the nonlinearity will be twofold: (i) to select a specific combination of modes within the almost-degenerated band (the time-independent coefficients in this modal combination imply that the modes are preserving their relative phases and amplitudes, which are denoted as amplitude and phase locking) and (ii) to pull the frequencies of the participating intraband modes to generate a single wavelength emission (a single-frequency emission of the participating modes is denoted here as frequency locking).

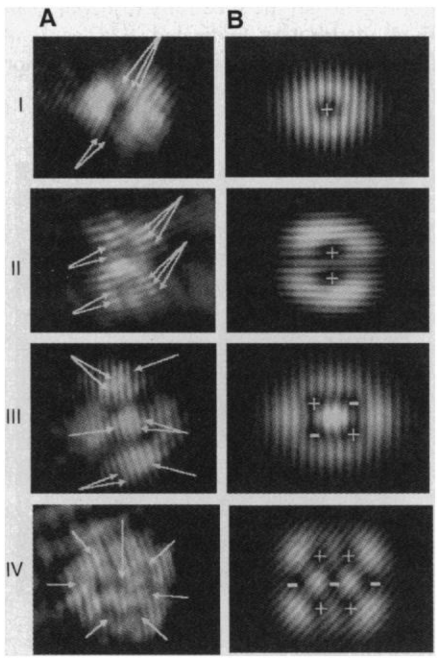

Fig. 6. Interference patterns. Experimental results (**A**) and the calculated interference. (**B**) I, doughnut mode; II, figure eight pattern; III, four-vortex array; IV, seven-vortex array.

The transverse electrical field in the microcavity was thus represented as a superposition of the modes belonging to a specific band (in order to achieve a single wavelength field), which yielded a set of rate equations for the modal coefficients. We used respective Gauss-Laguerre functions rather than the much more complicated hybrid mode functions (*14*), which can be justified because of the large cavity diameter, weak guiding properties, and paraxial propagation. These rate equations were solved numerically, using the parameters of (*15*), to obtain a steady-state solution for the coefficients of the Gauss-Lagurre functions within the chosen band for the given carrier density. A stable solution was achieved when the nonlinearities of the VCSEL caused the transverse modes to lock. The control parameters for the model were the current density J_0 and its lateral extent radius σ, normalized to the mode waist. The second parameter describes a varying local width parameter, depending on the injection conditions (*16*). When varying these parameters, a different combination of the band functions mode-locked, resulting in the generation of a different vortex array pattern.

The equations were solved for the first four Gauss-Laguerre wavelength-degenerated bands. The first band yielded conventional bright beams, but the second, third, and fourth families yielded patterns with vortice arrays similar to the experimentally observed patterns (Figs. 3B and 4B, respectively). These patterns were used for the calculation of the interference pattern of Fig. 6B. The calculated modes are also eigenfunctions of paraxial free space propagation (up to scale) (*14*); thus, the field distributions emanated from the nonlinear cavity were also preserved in the far field, which matches the experimental observations.

Having demonstrated the generation of optical vortex crystals in semiconductor microcavities and interpreted them as transverse mode locking within almost-degenerated wavelength families, several issues remain to be addressed. First, it is unclear from first principles why, out of the infinite possible linear combinations of the intraband modes, only the specific combinations described above were selected both experimentally and theoretically. Moreover, similar patterns and vortex arrays (although not as rich as shown here because of the higher Fresnel number of our experiment) were observed in another nonlinear optical system (*7*) incorporating a different type of nonlinearity and different dimensions and geometry. This similarity implies that the modal selection is of generic type and has little dependence on the specific parameters. Second, the CGL equation describing the nonlinear microcavity supports dark solitons (although the medium is self-focusing); and the ordered arrays of optical vortices, while propagating in the nonlinear cavity, can be modeled as arrays of dark (vortex) solitons. Their particlelike behavior, together with the possibility of deriving their soliton-soliton and soliton-device boundary forces, is a preferable direction for exploring the stability (and possibly the control) of these patterns.

We demonstrated the generation of complex spatial patterns and optical vortices crystals in broad-area VCSELs and showed that these patterns can be interpreted by the concept of transverse locking. The locking was possible because of the relatively small frequency spacing between specific modes of the cavity (almost wavelength-degenerated). The patterns appeared in both round and rectangular lasers, and they preserved their lateral distribution (with proper scaling) in the far field as well. The theoretical results revealed that the only combinations obtainable with the model of the VCSEL nonlinear cavity were the same specific mode combinations that were observed experimentally. The ability to spontaneously generate controlled and stable vortex arrays in a miniature cavity device is very appealing for applications of dynamic optical storage and processing.

References and Notes

1. V. Yu. Bazhenov, M. S. Soskin, M. V. Vasnetsov, *J. Mod. Opt.* **39**, 985 (1992); G. Indebetouw, *ibid.* **40**, 73 (1993); I. V. Basistiy, *et al.*, *Opt. Comm.* **103**, 422 (1993); J. F. Nye and M. V. Berry, *Proc. R. Soc. London Ser. A*, **336**, 165 (1974).
2. K. T. Gahagan and G. A. Swartzlander, *J. Opt. Soc. Am. B* **16**, 533 (1999).
3. W. J. Firth and A. J. Scroggie, *Europhys. Lett.* **26**, 521 (1994).
4. G. D'Alessandro and W. J. Firth, *Phys. Rev. A.* **46**, 537 (1992).
5. D. Michaelis, U. Peschel, F. Lederer, in *QELS'97* (Optical Society of America, Baltimore, MD, 1997), pp. 70–71.
6. W. J. Firth, A. J. Scroggie, G. S. McDonald, *Phys. Rev. A* **46**, R3609 (1992).
7. M. Brambila *et al.*, *ibid.* **43**, 5090 (1991).
8. M. Orenstein, *et al.*, *Appl. Phys. Lett.* **56**, 2384 (1990).
9. P. Coullet, L. Gill, F. Rocca, *Opt. Comm.* **73**, 403 (1989).
10. Ordered arrays of dark hexagons were predicted for Kerr medium by D'Alessandro and Firth (*4*).
11. G. P. Agrawal and N. K. Dutta, *Long Wavelength Semiconductor Lasers* (Van Nostrand Reinhold, New York, 1986).
12. J. Scheuer, D. Arbel, M. Orenstein, personal communication.
13. A. Yariv, *Optical Electronics* (Saunders, Philadelphia, PA, ed. 4, 1991).
14. The Gauss-Laguerre functions are the transverse solutions of the paraxial wave equation. The functions are

$$A_{p0}(r,\varphi) = \frac{2}{\sqrt{2\pi}} L_p^0(2r^2)\cdot e^{-r^2}; A_{plj}(r,\varphi) =$$

$$\frac{2}{\sqrt{2\pi}}(2r^2) = \left(\frac{p!}{(p+1)!}\right)^{1/2}\cdot L_p^1(2r^2)\cdot e^{-r^2}$$

$$\times \begin{cases} e^{+il\varphi} & j = 1 \\ e^{-il\varphi} & j = 2 \end{cases}$$

where $p = 0, 1, \ldots$ is the radial index; $l = 0, 1, \ldots$ is the angular index; r is the radial coordinate normalized by the beam waste; and $L^1{}_p$ is Laguerre polynomials. The electrical field is represented by $\varepsilon(t) = \sum_n E_n(t)\cdot\Psi_n(r,\varphi)$, where Ψ_n is the Gauss-Laguerre modes. The functions satisfying $2p + l$ = constant have the same propagation constant (that is, the same wavelength in the cavity) and form a wavelength-degenerated family.

15. L. A. Coldern and S. W. Corzine, *Diode Lasers and Photonic Integrated Circuits* (Wiley-Interscience, New York, 1995).
16. An additional control parameter, σ, is included in our analysis to correctly describe a local width imposed by either the boundary conditions or local inhomogeneity. The width parameter transforms the uniformly distributed spectral models of an unbounded problem into a banded spectrum. The almost-degenerated wavelength modes within each band are readily locked by the medium nonlinearity to form the complex field pattern. Both the lateral inhomogeniety and the complex nonlinear medium are the required ingredients for the pattern formation. This result is generally applicable to vortex formation in various fields of science. To the best of our knowledge, all such patterns reported previously (experimental and theoretical) were obtained in bounded nonlinear systems (including periodic boundaries) (*3,–6, 10*). The specific details of the width parameter in our system are related to the inhomogeneous pumping and thermally induced index gradient (thermal lensing) that are well known for semiconductor lasers.

17. We thank the Israel Ministry of Science and Technology for partially supporting this research and one of the reviewers for helpful remarks.

13 January 1999; accepted 1 June 1999

All-Polymer Optoelectronic Devices

Peter K. H. Ho, D. Stephen Thomas, Richard H. Friend, Nir Tessler*

Composites of nanoparticles and conjugated polymers that exhibit composition-tunable optical constants have been developed for use in semiconducting photonic structures. For example, the 550-nanometer wavelength in-plane refractive index of poly(p-phenylenevinylene)–silica composites can be tailored over the range of 1.6 to 2.7, allowing efficient distributed Bragg reflectors and waveguides to be fabricated. Low levels of chemical doping improve electrical conductivity through these structures without detriment to their photonic properties. Exemplifying these concepts, all-polymer microcavities and microcavity light-emitting diodes were demonstrated. Appropriate confinement of photons and electron-hole pairs in these organic semiconductor-based structures can be achieved.

Organic semiconductor devices are receiving considerable attention because of the immense tailorability and processing advantages of conjugated polymers (*1–4*). Recent developments in ink-jet printing, microcontact printing, and other soft lithographies (*5*) have further improved their potential for low-cost fabrication of large-area integrated devices on both rigid and flexible substrates. However, steps toward all-organic optoelectronic devices (*1, 2*) have been hampered by the lack of appropriate photonic building blocks that have a sufficient refractive index contrast and that can support a useful current density.

This is because, to a large extent, the index contrast between organic polymers is limited by the similar refractive powers of their constituent structural units (*6*). Even if the desired contrast can be obtained, the discontinuity of charge transport levels across the interface still potentially complicates carrier motion across the junction. Hence, there is an incentive to find a general scheme that allows the optical constants to be manipulated separately from other electronic and transport properties of the material.

One successful scheme is to form nanocomposites of the polymer with well-dispersed wide bandgap nanoparticles. The method comprises a microemulsion nanoparticle synthesis (*7*), followed by surface functionalization, and homogeneous blending with the polymer solution for subsequent processing. Using this approach, we obtained thin films of the semiconducting poly(p-phenylenevinylene)–silica (PPV-SiO_2) composite that combine a wide index tunability with little Mie scattering, in contrast to previous work (*8, 9*).

Although PPV and SiO_2 are selected because of their respective high (n_{550} = 2.3 to 2.7, depending on processing) and low (n_{550} = 1.45) refractive indices at a wavelength of 550 nm, the method can readily be generalized to include other matrix polymers (for example, polyfluorenes) and inorganic particles (for example, high-index ZrO_2). Repeated solution-deposition and insolubilization by thermal processing or cross-linking can then be used to

Cavendish Laboratory, Madingley Road, Cambridge CB3 0HE, UK.

*To whom correspondence should be addressed. E-mail: nt202@phy.cam.ac.uk